Airborne High Spectral Resolution Lidar for profiling aerosol optical properties

Johnathan W. Hair,[1,*] Chris A. Hostetler,[1] Anthony L. Cook,[1] David B. Harper,[1] Richard A. Ferrare,[1] Terry L. Mack,[2] Wayne Welch,[3] Luis Ramos Izquierdo,[4] and Floyd E. Hovis[5]

[1]National Aeronautics and Space Administration, Langley Research Center, Hampton, Virginia, 23681, USA

[2]Lockheed-Martin, Langley Research Center, Hampton Virginia, 23681, USA

[3]Welch Mechanical Designs, LLC., Havre de Grace, Maryland, 21078, USA

[4]National Aeronautics and Space Administration, Goddard Flight Research Center, Greenbelt, Maryland, 20771, USA

[5]Fibertek, Inc., Herndon, Virginia, 20170, USA

*Corresponding author: johnathan.w.hair@nasa.gov

Received 9 June 2008; revised 10 October 2008; accepted 14 October 2008; posted 23 October 2008 (Doc. ID 97183); published 12 December 2008

A compact, highly robust airborne High Spectral Resolution Lidar (HSRL) that provides measurements of aerosol backscatter and extinction coefficients and aerosol depolarization at two wavelengths has been developed, tested, and deployed on nine field experiments (over 650 flight hours). A unique and advantageous design element of the HSRL system is the ability to radiometrically calibrate the instrument internally, eliminating any reliance on vicarious calibration from atmospheric targets for which aerosol loading must be estimated. This paper discusses the design of the airborne HSRL, the internal calibration and accuracy of the instrument, data products produced, and observations and calibration data from the first two field missions: the Joint Intercontinental Chemical Transport Experiment—Phase B (INTEX-B)/Megacity Aerosol Experiment—Mexico City (MAX-Mex)/Megacities Impacts on Regional and Global Environment (MILAGRO) field mission (hereafter MILAGRO) and the Gulf of Mexico Atmospheric Composition and Climate Study/Texas Air Quality Study II (hereafter GoMACCS/TexAQS II).

OCIS codes: 010.0010, 010.1110, 280.0280, 280.1100, 280.1310, 280.3640.

1. Introduction

It has long been recognized that more information is needed on the distribution and optical properties of aerosols and clouds. Aerosols play a key role in the processes that govern climate through both direct radiative forcing, via scattering and absorption of solar radiation, and indirect radiative forcing, via altering the formation and albedo of clouds and precipitation. When attempting to account for how these direct and indirect aerosol radiative effects impact climate change, the Intergovernmental Panel on Climate Change concluded that the uncertainties associated with these aerosol radiative forcings were larger than the uncertainties associated with any of the other principal components of radiative forcing impacting climate change [1]. Aerosols also have a large impact on air quality and chemistry in the troposphere. Clouds play a major role in determining the Earth's climate, and our limited understanding of cloud-climate feedback processes leads to very large uncertainties in our ability to predict climate. Better information is needed on cloud optical properties and vertical distribution to develop improved cloud models for inclusion in climate models.

0003-6935/08/366734-19$15.00/0

Lidar is widely recognized as a necessary component in any strategy to provide the information on aerosol and cloud spatial distribution and optical properties required to address these outstanding issues.

The National Aeronautics and Space Administration (NASA) Langley Research Center (LaRC) airborne High Spectral Resolution Lidar (HSRL) Project was conceived with the goal of developing a compact, robust nadir-viewing airborne HSRL that could be employed on a variety of important aerosol and cloud related objectives, including providing accurate quantitative measurements of aerosol and cloud properties in the context of radiation- and chemistry-focused field missions, validating the Cloud-Aerosol Lidar with Orthogonal Polarization (CALIOP) on the Cloud-Aerosol Lidar and Infrared Pathfinder Satellite Observations (CALIPSO) satellite, and investigating the technologies required for and science benefits of a future spaceborne HSRL instrument [2,3]. The design and development of the instrument were initiated in the spring of 2000 and culminated in a complete instrument realization and initial ground tests in November 2004. The instrument was flown for the first time in December 2004 on a Learjet 25C operated by L3 Communications Flight International Aviation LLC. The instrument performed flawlessly in both the ground tests and the initial test flights. The system was later refined and reconfigured for deployment on the NASA LaRC's King Air B-200 aircraft along with two other remote sensing instruments, the Langley Airborne A-band Spectrometer (LAABS) and the HyperSpectral Polarimeter for Aerosol Retrievals (HySPAR). In 2008, LAABS and HySPAR were dropped from the payload and the NASA Goddard Institute for Space Studies (GISS) Research Scanning Polarimeter (RSP) instrument was flown with the HSRL. Since the instrument has been configured for the NASA LaRC B-200, it has flown in nine major field campaigns totaling over 650 hours of flight operations. The goal for codeployment of the additional instruments was to enable investigation of new remote sensing strategies involving combined active-passive retrievals, e.g., using HSRL extinction and backscatter coefficients and depolarization profiles to constrain oxygen A-band and photopolarimeter retrievals of aerosol optical and microphysical properties.

This paper discusses the design of the airborne HSRL instrument, some key instrument performance parameters, and data products from the first field experiment conducted with the instrument. In particular, this paper focuses on the unique and internal calibration technique that has been implemented and provides absolute measurements of the data products without the reliance on assuming a clear air or pure molecular atmosphere. An overview of the HSRL technique is given in Section 2. The instrument design is described in Section 3. The fundamental measurements and retrievals of aerosol and cloud properties are described in Section 4. The internal calibration subsystems and the calibration stability of the instrument are discussed in Section 5. In Section 6, HSRL data products from the joint MILAGRO field mission are presented. Calibration data and statistics from the GoMACCS/TexAQS II field campaign are also presented. Concluding remarks are presented in the final section.

2. Overview of the HSRL Measurement Technique

Standard backscatter lidars are commonly used to derive aerosol backscatter and extinction coefficients. However, a standard backscatter lidar actually measures *attenuated backscattered coefficients*, i.e., the product of the backscatter coefficient and the two-way transmission of the atmospheric volume between the lidar and the backscatter volume in question. The retrieval of both particulate extinction and backscatter coefficients relies on an assumption of their ratio, S_a [4–6]. Error in the assumed value of S_a creates errors in both the backscatter and extinction coefficient profiles. The actual value of S_a depends on particle composition, size distribution, and shape. The value of S_a can vary widely ($20 \le S_a$ (sr) ≤ 81 at 532 nm) (e.g., [7,8]) and, for any given observation or scene, can be difficult to estimate. For example, typical values for S_a (532 nm) are ~20–30 sr (marine aerosols), ~30–60 (desert dust), 35–65 (urban haze), 40–60 (smoke), 40–80 (Southeast Asian aerosols) [8].

The HSRL technique [9–16] takes advantage of the spectral distribution of the lidar return signal to discriminate aerosol returns from molecular returns and estimate aerosol extinction and backscatter coefficients independently. Airborne HSRL systems have been implemented previously [17,18] and, more recently, a HSRL system has been incorporated and demonstrated on the German Aerospace Center (DLR) Falcon research aircraft [19]. The HSRL technique relies on the difference in spectral distribution of backscattered signal from molecules and particulates (see Fig. 1, top panel). While light that is backscattered from aerosol particles has nearly the same spectral distribution as that of the incident laser pulse, the Cabannes scattering from air molecules is broadened by a few GHz [20–22].

Discrimination between aerosol/cloud and molecular returns in the airborne HSRL receiver is accomplished by splitting the returned signal into two optical channels: the *molecular backscatter channel*, which is equipped with an extremely narrowband iodine vapor (I_2) absorption filter to eliminate the aerosol returns and pass the wings of the molecular spectrum (see Fig. 1, bottom panel), and the *total backscatter channel*, which passes all frequencies of the returned signal [10,15]. After appropriate internal calibration of the sensitivities of the two channels, the signals are used to derive profiles of extinction, backscatter coefficient, and extinction-to-backscatter ratio, S_a. The molecular backscatter channel signal is first corrected for the

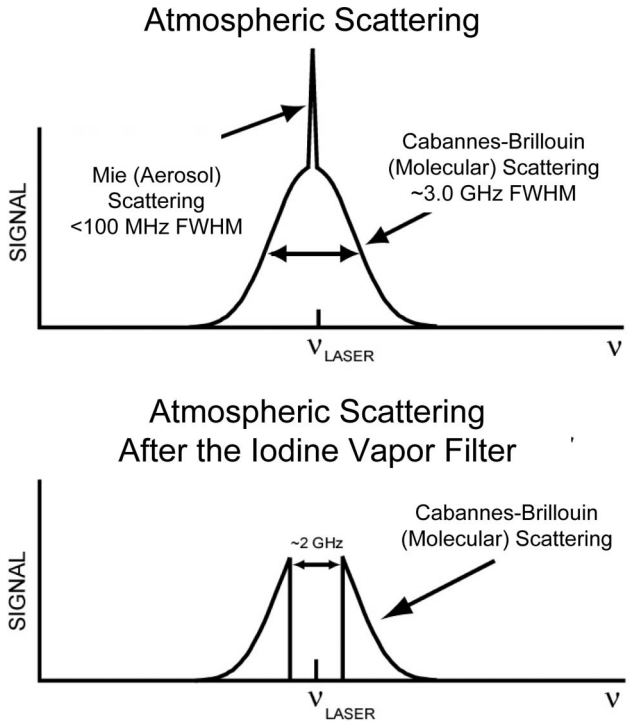

Fig. 1. Schematic diagram for a HSRL return spectra.

amount of molecular backscatter signal blocked by the I_2 filter. Aerosol extinction is then computed from the molecular signal channel by comparing the measured *attenuated* molecular backscatter coefficient profile, which is attenuated by aerosol and molecular extinction along the transmit–receive path, to a reference, unattenuated molecular backscatter coefficient profile that is calculated using molecular density profiles produced from radiosonde data or an assimilation model [9,23,24]. The volume backscatter coefficient (aerosol plus molecular backscattered signal) is computed by taking the ratio between the total scatter signal and the corrected molecular backscatter channel signal, and then multiplying by the molecular backscatter coefficient profile determined from the sonde- or model-derived molecular density profile. The aerosol backscatter coefficient is computed by subtracting the sonde- or model-derived molecular backscatter coefficient profile from the volume backscatter coefficient profile. The profile of S_a is computed from the ratio of the aerosol extinction and backscatter coefficient profiles.

3. Instrument Design

A. System Overview

The LaRC instrument employs the HSRL technique at 532 nm and the standard backscatter lidar technique at 1064 nm. In addition, it is polarization sensitive at both wavelengths. The fundamental data products are aerosol backscatter and extinction coefficients at 532 nm, aerosol backscatter coefficient at 1064 nm, and degree of linear polarization at both wavelengths. These basic measurements are used to compute several aerosol intensive parameters, including S_a, backscatter coefficient wavelength dependence, and aerosol depolarization ratio. The extinction profile is integrated vertically to produce aerosol optical depth along the flight track.

Figure 2 shows the basic architecture of the instrument. The instrument is designed to be compact and mechanically robust enough to enable deployment on small aircraft, as shown in Fig. 2 with the instrument installed on the NASA King Air. The telescope light-shield provides the structural backbone of the instrument. It is essentially a cylindrical optical breadboard to which the pulsed laser, transmit optics, and the telescope aft-optics are rigidly mounted. In addition to providing a mechanically robust assembly, this design approach makes it straightforward to add new or replacement subsystems or to reconfigure the instrument for installation on different aircraft platforms. The control and detector modules, shown in Fig. 2, are located in a separate rack in the rear of the picture.

As discussed above, the HSRL technique is based on the spectral discrimination of aerosol and molecular backscatter coefficients. This imposes requirements on the laser transmitter as well as the receiver. The laser must operate on a single longitudinal mode to ensure that the transmitted frequency distribution is significantly narrower than the molecular broadening of the backscattered signal. Also, because the LaRC system relies on the iodine vapor filter technique for spectral separation in the receiver, the transmitter must be capable of being tuned and locked to an iodine absorption feature. The transmitter in the LaRC system involves four subsystems: a pulsed Nd:YAG laser, a tunable dual-wavelength continuous-wave (CW) injection seed laser, an electro-optic feedback loop that locks the seed laser frequency to the center of the desired iodine line, and the transmitter optics module at the output of the pulsed laser. As shown in Fig. 3, the output of the 1064 nm CW Nd:YAG seed laser is coupled into a singlemode polarization-maintaining fiber that is then directly coupled into the pulsed Nd:YAG laser for injection seeding. The 532 nm CW output is used as a reference to tune and lock the seed laser frequency. The transmit optics module, Fig. 4, expands the pulsed output beam, linearizes the output polarization, provides a means to shutter the output, and automatically attenuates the output as dictated by the operational scenario, and provides a measurement of the pulsed laser spectral purity for each pulse using a separate iodine vapor cell.

The receiver involves five subsystems: a Newtonian telescope, an aft-optics module mounted near-kinematically to the telescope, detector modules for the standard backscatter and depolarization channels, an iodine filter module for molecular/aerosol discrimination at 532 nm, and a data acquisition and control computer. The aft-optics module optically separates wavelengths, polarization states, and, at 532 nm, the molecular and total backscatter

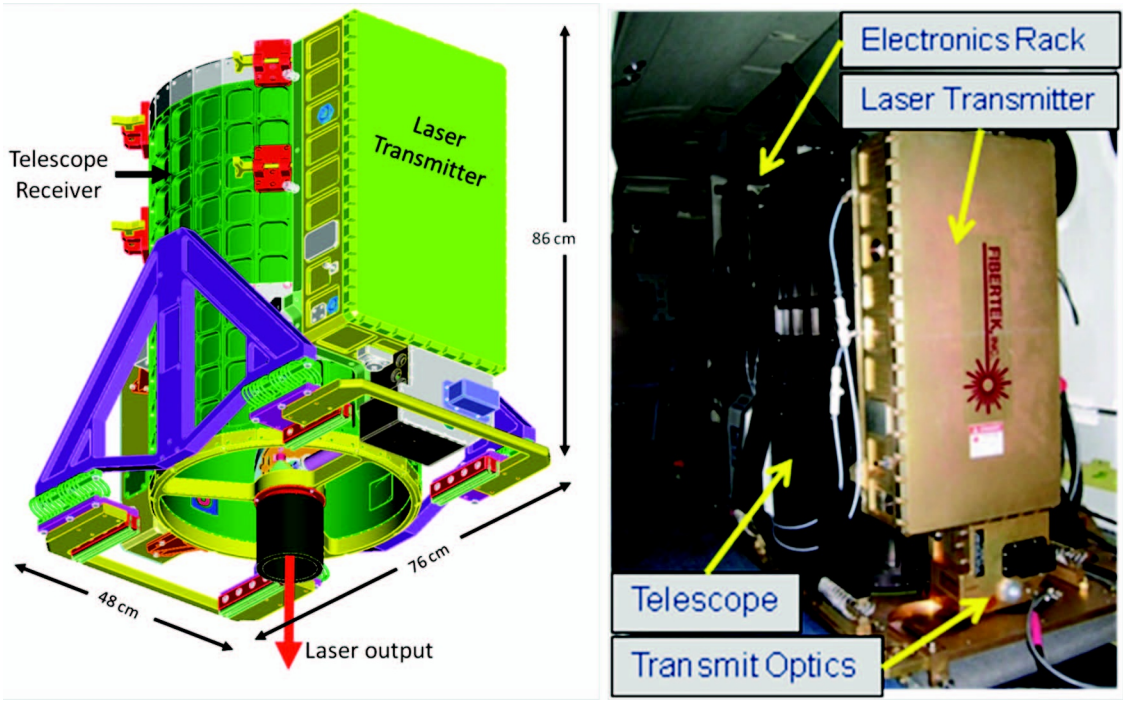

Fig. 2. Instrument model and overall dimensions (76 cm × 48 cm × 86 cm) showing the main components of the Airborne HSRL instrument; the laser transmitter, telescope, and the transmit optics. The electronics rack (106 cm) which contains the PXI data acquisition computer, seed laser, all detectors, iodine cells for filtering and monitoring spectral purity, and power supplies for the lasers is shown in the photo behind the main system.

channels. The various optical signals are fiber-optically coupled from the aft-optics module to the respective detectors-amplifier modules, as is the light to the iodine vapor filter module. Descriptions of the key transmitter and receiver subsystems are discussed in the following subsections.

B. Laser Transmitter

The pulsed output laser is a custom-designed injection-seeded Nd:YAG system developed by Fibertek, Inc. of Herndon, Virginia [25]. It provides output beams at the fundamental (1064 nm) and second harmonic wavelengths (532 nm). The injection seed laser is a tunable Prometheus Nd:YAG nonplanar ring oscillator laser built by Innolight GmbH. In addition to providing a CW source for seeding the pulsed laser at 1064 nm, the seed laser also provides a CW output at 532 nm. The Innolight laser can be tuned over ~90 GHz at 532 nm and has a continuous,

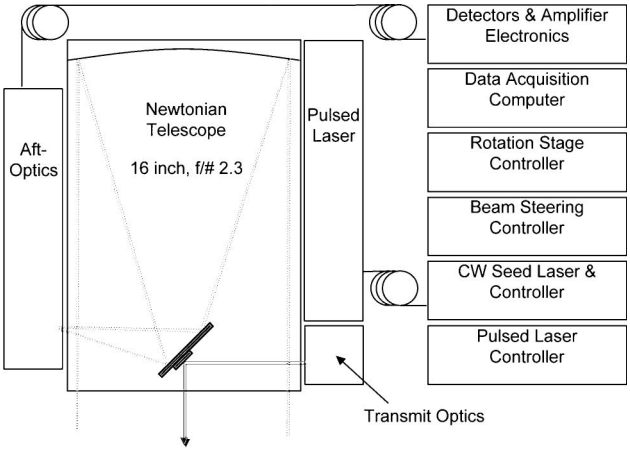

Fig. 3. Basic layout of the HSRL showing the optical and electronic subsystems.

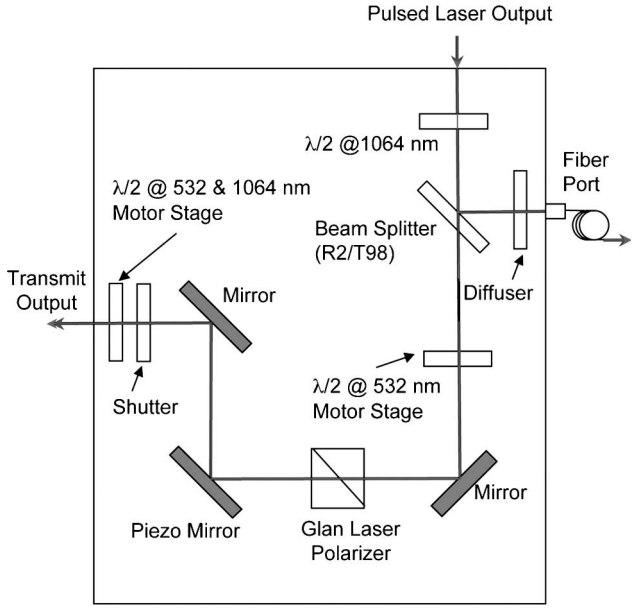

Fig. 4. Schematic of the transmit beam optical layout. The Glan laser polarizer ensures linear polarization output. The output polarization for both wavelengths can be set relative to the receiver with the last half-wave plate before transmission in to the atmosphere. A fiber pickoff is shown for the energy and spectral purity monitor which are housed in a separate module.

mode-hop-free scanning range of ~12 GHz. The frequency agility of the seed laser allows the CW 532 nm output to be used in an electro-optic feedback loop designed to lock the seed laser frequency to an iodine absorption line and, in a calibration mode, to determine the transmission of the iodine vapor cell as a function of wavelength. The basic parameters of the laser systems are provided in Table 1. Both laser systems are operated at ~25 C, providing output wavelength control near 532.242 nm, the wavelength of the strongest absorption line in the iodine spectrum within the Nd:YAG tuning range [26,27]. Of the available absorption lines in the tuning range of the transmitter, the strongest line was chosen to maintain high aerosol backscattered light rejection at the laser wavelength while minimizing the iodine density in the receiver filter. Lowering the iodine gas number density, and therefore the operational temperature and vapor pressure, minimizes both the collisional broadening of the absorption line and broadband continuum absorption [26,27], thereby providing the maximum transmission of the wings of the broadened molecular backscattered signal. Other considerations contributing to the choice of this particular line included the facts that the measured pulsed laser spectral purity and the mode-hop-free tuning range of the seed laser were optimal for this line.

The pulsed laser is injection seeded using a modified ramp-and-fire technique [28–31] to ensure that every laser shot fires with high spectral purity at the appropriate wavelength when operating in the challenging vibrational environment of an aircraft. A total of 350 mW of CW 1064 nm power is used for seeding and is coupled into the pulsed laser via the high reflector mirror in the pulsed laser cavity. After accounting for losses through the high reflector mirror, approximately 10 mW of seed light is injected into the pulsed laser cavity. The injection seeding optical setup and the ramp-and-fire technique

Table 1. Basic Operational Parameters for the Pulsed and Seed Lasers

Parameter	Value
Pulsed Laser Transmitter	
Manufacturer	Fibertek, Inc.
Type	Custom Seeded Nd:YAG
Laser Repetition Rate	200 Hz
Wavelengths	532 nm, 1064 nm
Energy (after transmit optics)	2.5 mJ @ 532 nm 1.1 mJ @ 1064 nm
Polarization @ 532 nm and 1064 nm	Linear (>100:1)
Spectral Purity Ratio[a]	>5000:1 @ 532 nm
Pulse Temporal Width	15 ns @ 532 nm
Pulse Spectral Width	38 MHz @ 532 nm
Laser Divergence @ 532 nm and 1064 nm	0.8 mrad (nominal)
Beam Diameter @ 532 nm and 1064 nm	3 mm, 6 mm (nominal)
Seed Laser	
Manufacturer	Innolight, GmbH
Type	Prometheus, Nd:YAG
Wavelengths	532 nm, 1064 nm
Power	30 mW @ 532 nm >750 mW @ 1064 nm
Tuning Range	>90 GHz @ 532 nm
Continuous Tuning Range	10–12 GHz @ 532 nm

[a]As defined in text.

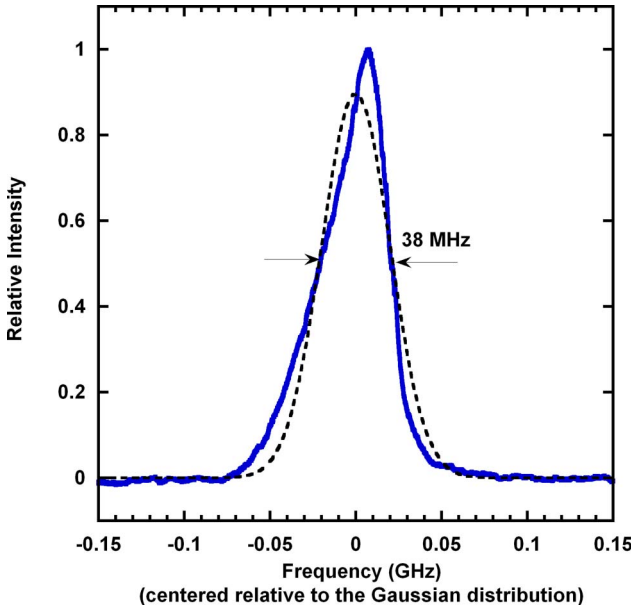

Fig. 5. (Color online) Pulsed laser spectral lineshape measured at 1064 nm. The frequency scale is referenced to the center of the best fit of a Gaussian distribution lineshape shown as a dashed line. The full width at half-maximum of the Gaussian fit is 38 MHz.

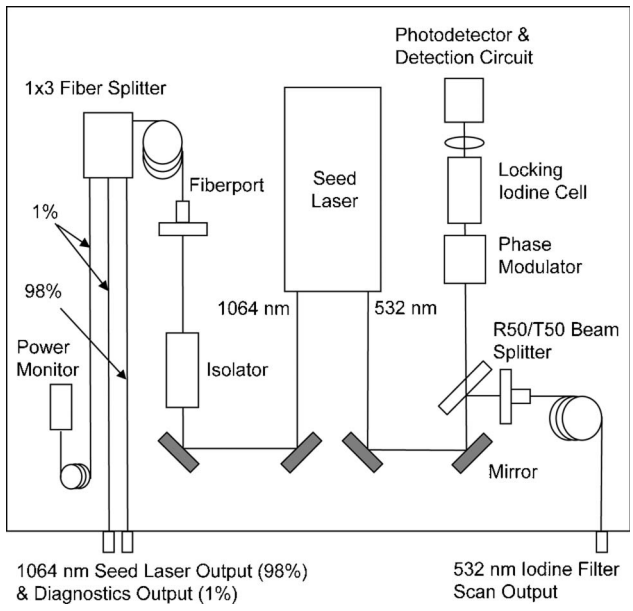

Fig. 6. Diagram providing the basic layout for the seed laser with dual-wavelength outputs. The 532 and 1064 nm output optical paths for the energy monitor, laser line locking to an iodine cell, and filter scan output are shown. There are two outputs for the 1064 nm laser light. Approximately 98% is directly coupled with a PM fiber to the pulsed laser used for seeding. The 1% output is used for diagnostics and as a frequency marker for the iodine filter scans using a 300 MHz confocal interferometer.

implemented are described in detail by Hovis *et al.* [25]. The laser spectral lineshape has been measured using a confocal interferometer with a 600 MHz free spectral range and has an estimated full width at half-maximum (FWHM) of 38 MHz, as shown in Fig. 5. In addition, the ramp-and-fire implementation has a relative phase adjustment to fire the q switch based on the resonant fringe, which is set by simultaneously injecting the pulsed and seed laser outputs into the confocal interferometer to match the seed laser to the pulsed laser output to within <5 MHz. This confirms that the frequency of the seed laser, which is used for frequency stabilization, matches the pulsed laser output frequency.

C. Seed Laser Frequency Control

The seed laser frequency is controlled by a high-speed, autonomous electro-optic control loop that is based on a phase modulation technique [32–34]. Figure 6 shows a basic block diagram of the seed laser and the elements of the frequency control loop. The control system senses the wavelength of the CW 532 nm seed laser output with respect to the position of the iodine absorption line and tunes the seed laser to center the 532 nm output on that line. This technique was chosen over alternate techniques that rely on the pulsed laser output for frequency sensing and control, as it is much more accurate and reliable. Of the total 30 mW of CW 532 nm light from the seed laser, approximately 5 mW is coupled to a multimode fiber for delivery to the receiver where it is used to measure the spectral transmission of the iodine vapor filter in the receiver as discussed in more detail in Subsection 5.A. Approximately 1 mW of the 532 nm light is directed to the frequency locking system, which consists of three main components: a 240 MHz phase modulator, an iodine cell (separate from the iodine cell in the receiver), and detection and control electronics. The phase modulator is a New Focus Model 4001 driven at 240 MHz by a resonant tank circuit. The custom locking cell was fabricated by Innovative Scientific Solutions with a fixed number density of iodine within the 1 in. diameter by 2 in. long Pyrex cell [35]. The cell is temperature controlled at 35 C $\pm$ 1 C, which is sufficient to ensure the iodine remains completely in the gas phase. The transmission spectrum of the locking iodine cell has an online transmission of $\sim$29% for the absorption line centered near 532.242 nm at which we currently operate the transmitter, see Fig. 7. The detection and control system consists of a model FND-100 silicon detector from Perkin-Elmer, compact custom-built amplifier, phase-detection circuits, and mixing circuits. The output of the amplifier consists of the sum of two beat signals: the beat signal between the +240 and −240 MHz shifted optical signals with the unshifted optical signal. These two signals are both sinusoidal at 240 MHz, but 180° out of phase. The amplitude of the resulting sum is zero when the amplitudes of the two shifted optical signals are equal, i.e., when the unshifted optical signal

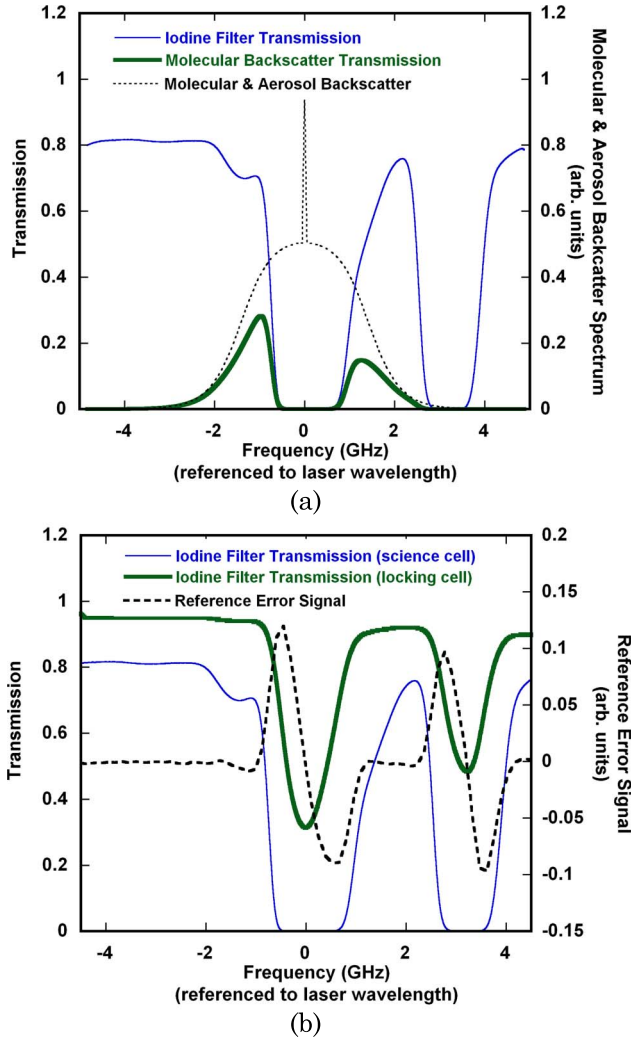

Fig. 7. (Color online) (a) Measured transmission function of the main science channel iodine vapor filter using the 532 nm output from the seed laser is shown as the solid thin line. The Cabannes–Brillouin backscattered signal spectra (275 K, 0.75 atm.) with Mie scattering included is plotted as the dashed line. The filtered transmitted backscattered spectrum is shown as the solid thick line. (b) Thin solid line, measured transmission function of the main science channel iodine vapor filter. The measured filter transmission function of the iodine locking cell is shown as a solid thick line, and the error signal from the locking circuit is shown for reference as the dashed line.

is nearly centered in frequency on the iodine absorption feature. Note the locking frequency does not occur exactly at the center of the absorption line due the asymmetry induced from nearby absorption lines. Note also that the locking frequency is referenced to the filter transmission based on the scan data described in Section 5.A below. The error signal is recorded simultaneously with the scan of the filter transmission. The phase detection circuit closely follows that of Bjorklund, 1980 [34] and shifts the phase of the resultant 240 MHz signal from the photodetector amplifier to match that of the local oscillator signal injected at the mixer. The output of the mixer is a DC error signal that is proportional to the energy in the resultant of the 240 MHz beat signals. The error

signal, shown in Fig. 7(b), is directly coupled to a dual-loop proportional-integral-derivative (PID) circuit to provide control feedback to the seed laser that effectively equalizes the +240 and −240 MHz optical sidebands downstream of the iodine filter, thereby centering the 532 nm seed laser output on the center of the chosen iodine absorption line. The seed laser frequency is adjusted with a fast tuning piezo transducer custom-mounted in the seed laser, and the second slower PID loop maintains the transducer voltage near zero by adjusting the seed laser temperature. The error signal is recorded during scans of the iodine filter transmission curve described in Section 5.A. All data are taken simultaneously during the scan and then scaled to frequency, thereby creating a transfer function of the error signal from voltage to frequency. Using this transfer function, this configuration has been shown to provide long-term frequency stability to within 0.1 MHz (RMS) during flights, which far exceeds the requirements imposed by the HSRL technique.

Figure 6 also shows the 1064 nm optical path, which incorporates a high-power isolator to prevent backreflected light from affecting the performance of the frequency locking loop. The 1064 nm beam is coupled into a polarization-maintaining (PM) single-mode fiber and is subsequently split into three channels using a 1×3 PM fiber splitter made by Canadian Instrumentation and Research Ltd. The split ratios of the 1×3 splitter are 98%, 1%, and 1%. The 98% output is coupled into a single-mode PM fiber which is then directly coupled into the pulsed Nd:YAG laser for injection seeding, while the 1% legs are used for diagnostics and for frequency scaling the spectral scans of the iodine cell using a confocal interferometer.

D. Transmit Optics and Spectral Purity Monitor

The transmit optics assembly is mounted directly to the pulsed laser housing and provides several important functions for the lidar system. A layout of the optical components is provided in Fig. 4. The two coaligned beam-expanded outputs of the pulsed laser are first sent through a 1064 nm half-waveplate (full wave at 532 nm) and a then a 532 nm half-waveplate (1064 nm full-waveplate) to coalign the two laser output polarizations to a Glan-laser polarizer, which is used for two functions: (1) insuring high polarization purity of the laser output, and (2) providing an attenuation mechanism to reduce the energy of the 532 nm output when required for eye safety. The attenuation function is implemented by rotating the 532 nm half-wave plate to detune the axes of polarization of the laser output at 532 nm from the pass axis of the polarizer, and is automatically adjusted as a function of aircraft altitude. The laser divergences of the two beams are adjustable using a telescope mounted inside the laser housing and are nominally set to 0.8 mrad. A small fraction of the pulsed laser light is picked off into a 1 mm multimode fiber for diagnostics that include measuring the spectral purity of the 532 nm light and the energy at both wavelengths. A coarse mirror before the polarizer is used to align the output beam in the lab before integration on the aircraft. A high resolution ($<2\,\mu$rad) piezo mirror (Mad City Labs, model Nano-MTA2) is used to provide accurate, quasi real-time boresighting of the laser output to the receiver field-of-view (FOV). A final dual-wavelength half-waveplate on a motor stage is used to align the polarization axis of the transmitted output with that of the receiver polarization analyzers.

A unique and important feature of the airborne HSRL system is the spectral purity monitoring subsystem. In this subsystem, pulsed 532 nm laser output from the transmitter is directed via fiber to a separate iodine cell (the "spectral purity cell") to determine the spectral purity of each laser shot. The spectral purity cell is built using a 25 mm diameter by 50 mm long quartz cell that has a fixed density of iodine and is temperature controlled to 65 C, at which point the iodine is completely in the gas phase. While the spectral purity cell is two times shorter than the main iodine cell, it contains twice the iodine density as that of the main iodine cell described in Section 5.A below and has a centerline transmission at 532.242 nm less than 10^{-6}. The spectral widths, ~2.0 GHz at the 50% transmission points, of the two cells are comparable since they are operated at the same temperature. While pressure broadening is higher for the spectral purity cell, for the densities and temperatures at which the cells are operated, the relative increase in spectral width is negligible.

The pulsed laser light passes through the spectral purity cell, and the transmitted pulse amplitude is determined. Single longitudinal mode laser shots centered in frequency on the iodine absorption line suffer high attenuation in the cell. Note, measurements of the temporal shape of the weak transmitted unseeded component through the spectral purity cell clearly show the mode beating that highlights the broadband component is observed. Shots that are not spectrally pure, i.e., that have energy in other longitudinal modes, result in a much higher signal at the detector, as any other modes are well outside the iodine absorption line. Before integration onto the aircraft, a separate calibration is performed with the laser frequency tuned off of the iodine absorption line to measure the overall electro-optical calibration constant of the subsystem for normalization. A threshold is then set on the detection circuit to prevent laser shots that are above a preset spectral purity level from being recorded in the data acquisition system. For unseeded laser shots, the increased throughput is orders of magnitude more than well-seeded laser shots. Typically, spectral purity ratios (i.e., the ratio of energy inside the iodine line to that outside the line) are greater than 5000:1 for this transmitter and, under certain conditions, have exceeded 10,000:1. The spectral purity monitoring system also provides a quantitative measurement

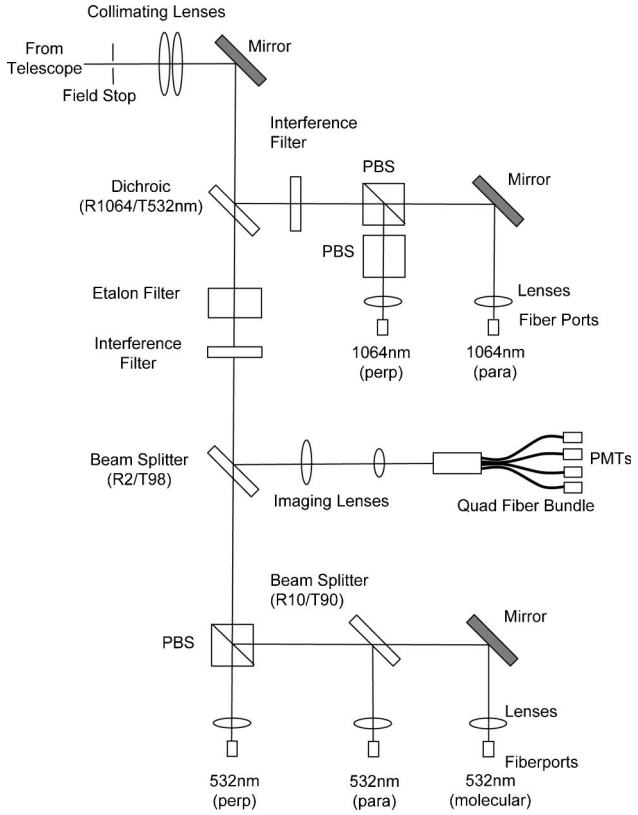

Fig. 8. Schematic showing the receiver optics connected to the output of the telescope. There are three different receiver legs consisting of the 1064 nm channels, 532 nm channels, and the quad-fiber boresighting channels. All output channels are fiber-coupled to the detectors and iodine vapor filter for the 532 nm molecular backscatter channel.

of the percent of laser shots seeded during aircraft operations. This system has successfully flown on two different aircraft, and the percent of unseeded shots is extremely low, with those few unseeded shots occurring mainly during takeoff and landing.

E. Telescope Receiver and Aft-optics

The telescope for the instrument is a 40 cm diameter $f/2.3$ Newtonian telescope designed, assembled, and aligned by Welch Mechanical Designs, LLC. The collected light is sent through a field stop that can be varied between 0.25 and 1.00 mrad and is then collimated through the aft-optics module. A diagram of the aft-optics module is provided in Fig. 8, and the main specifications of the receiver are given in Table 2. A dichroic beam splitter separates the 1064 and 532 nm optical signal channels. Another beam splitter in the 532 nm path directs 2% of the 532 return to a boresighting subsystem, with the remaining 98% going to the science channels.

Downstream of the dichroic beam splitter, the 1064 nm return passes through a 0.4 nm FWHM interference and solar blocking filter manufactured by Barr Associates. This filter has a peak transmission of 79%. A polarization beam splitting (PBS) cube is used to separate the two orthogonal polarizations of the backscattered light, denoted as 1064 nm *para* and 1064 nm *perp* in Fig. 8 for the parallel and perpendicular components, respectively. A second cube is used in the perpendicular channel to remove the residual ~5% parallel polarized signal in that optical channel.

The 532 nm light passes through a solid Fabry–Perot etalon (FWHM = 60 pm, free spectral range = 0.75 nm) and an interference filter (FWHM = 0.75 nm) that rejects out-of-band fringes from the etalon. The etalon is temperature tuned to match the laser wavelength and has a peak optical transmission of 82%. The interference and solar blocking filter have a combined optical transmission of 89%. A small fraction (~2%) of the 532 nm light is split off to the boresighting subsystem. The remaining ~98% of the 532 nm light is separated into the two orthogonal polarizations using a single PBS cube that is custom designed to provide high contrast (10000:1) and low cross talk between both polarization channels labeled as 532 nm *para* and 532 nm *perp* in Fig. 8. The parallel polarized light is split into two channels with a 90:10 beam splitter: the larger of the optical signals, denoted the 532 nm *molecular*, is directed to the iodine filter assembly and the smaller to a detector assembly identical to that of the perpendicular channel.

Except for the 95% parallel polarization channel at 532 nm, all science channels are coupled via 1 mm diameter solid-core fibers to detector modules shown in Fig. 9. In the detector modules, the returns are collimated, passed through a wedge/Lyot depolarizer, further split by a 95:5 beam splitter, and finally

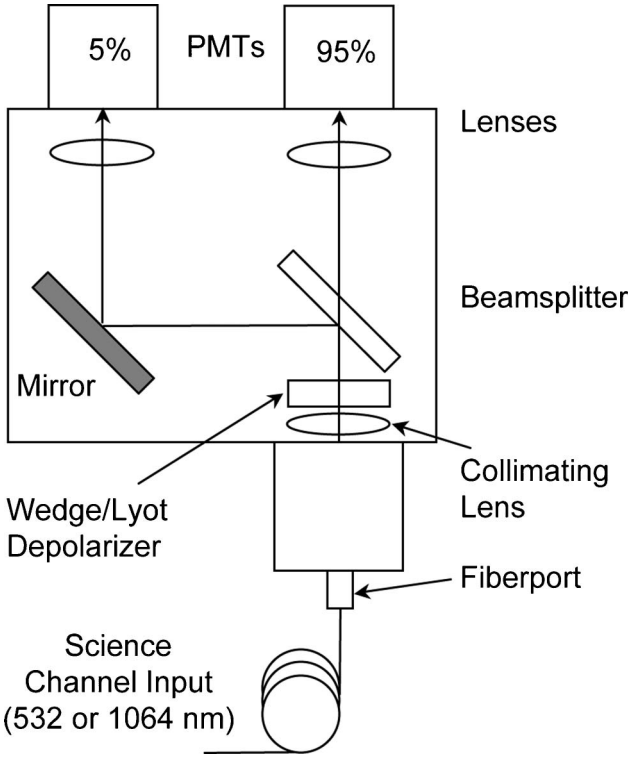

Fig. 9. Detector modules that incorporate fiber-coupled inputs and 5%–95% optical splits for high signal and low signal detectors.

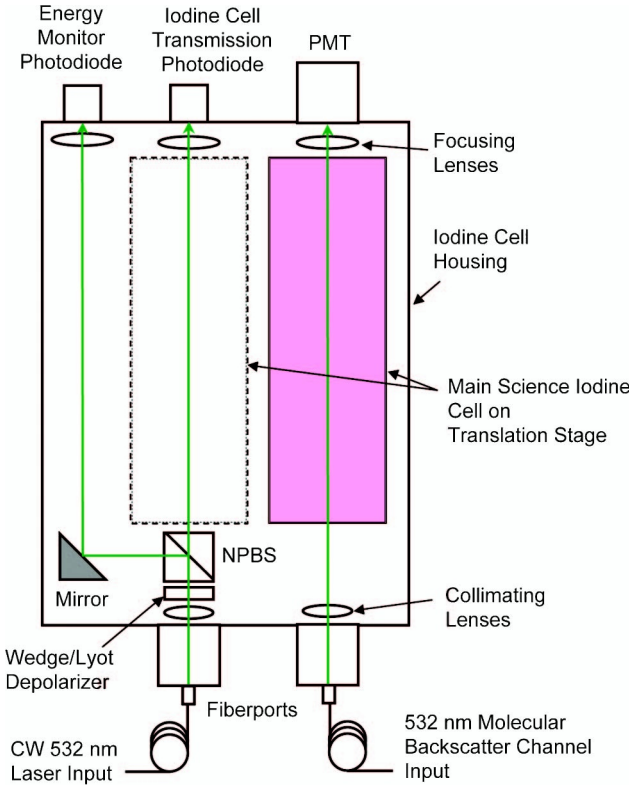

Fig. 10. Block diagram of the iodine vapor filter and the optical layout to provide periodic measurements of the filter transmission. The science channel input and the input to measure transmission spectra are both fiber-coupled.

focused onto detectors. Detection at 532 and 1064 nm is accomplished with photomultiplier tubes (PMTs) and avalanche photodiodes (APDs), respectively. The optical split into 5% and 95% channels is implemented to increase the dynamic range of the instrument.

The 532 nm molecular backscatter channel is fiber-coupled into the iodine filter module that contains the iodine vapor filter, additional inputs and mechanisms for calibration, and science and calibration detectors. The science detector is a PMT identical to that in the 532 parallel and perpendicular channels. A diagram of the 532 nm molecular backscatter channel detector module is shown in Fig. 10. The iodine filter and methods implemented for calibration are discussed in Section 5.

The boresighting subsystem provides near real-time control of the alignment between the transmitter and receiver. In the aft optics, the boresighting channel reimages the telescope field stop onto a quad-fiber bundle. Each quadrant consists of hundreds of 25 μm diameter fibers that are terminated in a SMA fiber connector and coupled to separate PMT detector modules, which are similar to the science channels but with smaller electronic bandwidths set to obtain higher signal-to-noise and a vertical resolution of $\sim$0.5 km. The signals from the four PMTs, corresponding to the four quadrants of the field stop image, are combined in a way to provide a feedback signal to an encoded piezo-electric actuated turning mirror (Mad City Labs) used to align the output laser beams to the center of the field stop. A separate manuscript is in preparation that more fully describes the details and performance of the boresight system. Initial analysis indicates that the boresight stability is within 10 μrad throughout a flight.

F. Data Acquisition and Control Electronics

The data acquisition system is designed to provide complete control, diagnostics, and calibration of the instrument without additional ground support hardware. All parameters and control commands are input to a master laptop computer; no manual adjustments are required for instrument operation. An Iridium satellite modem provides real-time communication and data downlink between the aircraft operator and the scientists on the ground.

The laptop computer interfaces to a National Instruments PXI chassis with a real-time PX-8176RT controller that controls all instrument function and manages data acquisition. The PXI chassis contains four PXI-6115 12 bit digitizers that have four channels per digitizer providing a total of 16 available channels. The HSRL system utilizes ten of these channels for the science data. Additionally, four channels are used to measure the quad PMT outputs from the boresight system. All 14 channels are typically averaged over 100 shots (0.5 s) and then transferred to the laptop computer for recording, analysis, and display. Before averaging, each channel is preprocessed to evaluate potential digitizer saturation, which is then denoted in the data stream. In postprocessing, saturated signals on the 90% optical channels (e.g., strong cloud signals) are substituted with gain-corrected signals from the 5% channels. Digital outputs from the PXI-6115 digitizer modules control the custom-built variable gain and offset amplifiers in the APD and PMT detector modules. The PXI chassis also includes a multifunction PXI-6052 data acquisition card for AD/DA input and output for recording and control of various system parameters such as the pulsed laser energies and position control of the calibration mechanisms. A PXI-4351 card is used to monitor various temperatures in the system for health and status. A PXI-6602 counter/timer card with an 80 MHz time base is used to provide synchronization of the digitizer triggers, laser energy monitors, and spectral purity monitor to within 12.5 ns of each output laser pulse.

The half-wave plates that control the orientation of the output laser polarization and the laser attenuation are mounted in encoded Newport (model PR50) rotation stages that are controlled via a GPIB interface. These stages provide robust, relatively fast, and accurate rotational adjustment for both calibration operations discussed below and attenuation of the laser for maintaining eye-safe operations.

4. Retrievals

There are five optical channels in the airborne HSRL system, three at 532 nm and two at 1064 nm, as shown and as labeled in Fig. 8. The background-subtracted backscattered signal in the three 532 nm channels is listed in Eq. (1), where P_{i2} is the filtered molecular scattering channel and $P_{\text{tot}}^{\parallel}$ and $P_{\text{tot}}^{\perp}$ are the total backscatter (i.e., molecular plus aerosol) parallel and perpendicular channels, respectively. The background-subtracted signal in the two 1064 nm channels is listed in Eq. (2), following a similar naming convention. The background signal is determined from the average of samples over a range in the profile that is beyond that corresponding to the Earth surface return and, therefore, absent of any laser backscattered signal. Since the linear depolarization is analyzed in the system at both wavelengths, the volume backscatter coefficient is separated in the parallel and perpendicular components in Eqs. (1) and (2). In these equations, β is the volume backscatter coefficient for molecular (m) scattering (Cabannes only) or aerosol (a) scattering; r is the range from the lidar; C represents system constants, which incorporate the power-aperture product and the optical and detector efficiencies; T is the one-way atmospheric transmission to range r; F is the transmission of the molecular scattering through the iodine filter; and Ψ is the transmitter-to-receiver overlap function. F is dependent on the atmospheric temperature and pressure [13,20,21]:

Table 2. Receiver Optical Specifications and Measured Optical Efficiencies

Parameter	Value
Telescope	
Manufacturer	Welch Mechanical Designs, LLC.
Clear Aperture, $F/\#$	40 cm, $F/\#2.3$
Type	Newtonian
Full Field of View	0.25–1.0 mrad (adjustable)
Receiver Optics	
Etalon Filter Manufacturer	Coronado
Etalon Filter Bandpass	60 pm FWHM @ 532 nm
Etalon Filter Efficiency	82% @ 532 nm
Interference Filter Manufacturer	Barr Associates
Interference Filter Bandpass	0.75 nm FWHM @ 532 nm 0.4 nm FWHM @ 1064 nm
Interference Filter Efficiency (with blocking filter)	89% @ 532 nm 79% @ 1064 nm
Detectors	PMT, Hamamatsu R7400U-20 QE = 18% @ 532 nm APD, EG&G C30955E-TC QE = 40% @ 1064 nm
Overall Optical Efficiency (excluding detectors)	57% @ 532 nm 54% @ 1064 nm

532 nm *Channels*

$$P_{i2}^{\parallel} = \frac{C_{i2}^{\parallel}}{r^2} F \beta_m^{\parallel} T^2 \Psi, \qquad P_{\text{tot}}^{\parallel} = \frac{C_{\text{tot}}^{\parallel}(\beta_m^{\parallel} + \beta_a^{\parallel})}{r^2} T^2 \Psi,$$

$$P_{\text{tot}}^{\perp} = \frac{C_{\text{tot}}^{\perp}(\beta_m^{\perp} + \beta_a^{\perp})}{r^2} T^2 \Psi, \tag{1}$$

1064 nm *Channels*

$$P_{\text{tot}}^{\parallel} = \frac{C_{\text{tot}}^{\parallel}(\beta_m^{\parallel} + \beta_a^{\parallel})}{r^2} T^2 \Psi,$$

$$P_{\text{tot}}^{\perp} = \frac{C_{\text{tot}}^{\perp}(\beta_m^{\perp} + \beta_a^{\perp})}{r^2} T^2 \Psi, \tag{2}$$

$$\beta_m \equiv \beta_m^{\parallel} + \beta_m^{\perp}, \qquad \beta_a \equiv \beta_a^{\parallel} + \beta_a^{\perp}. \tag{3}$$

Noted here and reflected in Eq. (2), by including only the molecular backscatter coefficient for the filtered channel ($P_{i2}^{\parallel}$), the iodine cell essentially filters out the entire aerosol backscattered signal for this particular system. This is due to the very high on-line attenuation of the receiver iodine cell (10^{-6}) and the high spectral purity of the laser. Also note that the spectral bandpass of the interference filter (see Table 2) for the 1064 nm channel is 0.4 nm and the etalon and interference filter for the 532 nm channel is 0.06 nm, thus transmitting only the Cabannes back scattering [22].

The 532 nm aerosol backscatter coefficient is determined using all three of the return signals in Eq. (1), as shown in Eq. (4), where G_{i2} and G_{dep} are the combined optical and detector gain ratios between the total parallel channel and molecular backscatter channel and between the polarization channels, respectively, as shown in Eq. (5), and δ_m is the molecular backscatter depolarization ratio as defined in Eq. (6). Given the spectral bandpass of both channels, only the Cabannes scattering is detected and the theoretical value of the molecular depolarization in the retrievals is $\delta_m = 0.0036$ [12]. It is noted that, in practice, a small amount of depolarization is induced in the receiver and it is observed that the nominal minimum value is near 0.0085 for this system. This value is used in the retrievals for the molecular depolarization value. The molecular backscatter coefficient (Cabannes scattering only) [22,36], $\beta_m = N d\sigma_\pi/d\Omega$, where $d\sigma_\pi/d\Omega = 5.931 \times 10^{-32}\ \text{m}^2\ \text{sr}^{-1}$ ($3.592 \times 10^{-33}\ \text{m}^2\ \text{sr}^{-1}$) at 532 nm (1064 nm) in Eq. (4), is estimated from molecular density, N, determined from an assimilation model or radiosonde data. As with the 532 nm channel, the gain factor between the parallel and perpendicular channels for 1064 nm is defined in Eq. (5). A detailed description of the method used to determine gain ratios G_{i2} and G_{dep} in Eq. (5) is provided in Section 5.

$$\beta_a = \beta_m \left[\frac{1}{(1+\delta_m)} \frac{F}{G_{i2}} \left(\frac{P_{\text{tot}}^{\parallel}}{P_{i2}^{\parallel}} + \frac{P_{\text{tot}}^{\perp}}{G_{\text{dep}} P_{i2}^{\parallel}} \right) - 1 \right], \tag{4}$$

$$G_{i2} \equiv \frac{C_{\mathrm{tot}}^{\parallel}}{C_{i2}^{\parallel}}, \qquad G_{\mathrm{dep}} \equiv \frac{C_{\mathrm{tot}}^{\perp}}{C_{\mathrm{tot}}^{\parallel}}, \tag{5}$$

$$\delta_m \equiv \frac{\beta_m^{\perp}}{\beta_m^{\parallel}}. \tag{6}$$

The 532 nm aerosol extinction coefficient, α_a, is determined from the molecular backscatter channel return, the measured iodine filter transmission, and the molecular extinction coefficient α_m, as shown in Eq. (7). The molecular extinction coefficient is calculated from the modeled or sonde-derived molecular density profile, N, and the total molecular cross section, $\sigma = 5.168 \times 10^{-31}\,\mathrm{m}^2$ ($3.1247 \times 10^{-32}\,\mathrm{m}^2$) for 532 nm (1064 nm) from Bucholtz [36]. The system overlap function, ψ, can be ignored by starting the retrieval 1.5 km from the aircraft where the overlap is very near unity. Alternatively, the overlap can be determined experimentally [37] from regions of clear air in the near field during flight, where clear air can be determined from the 532 nm aerosol backscattered signal that does not depend on the overlap function. The near-range (<1.5 km) overlap correction for the airborne HSRL is currently being assessed to determine its stability over a single flight and from flight to flight. Because of the observed accuracy and stability of the autonomous boresighting system, we have deduced that the overlap function is stable to within an extinction error of $0.01\,\mathrm{km}^{-1}$ for a range greater than 600–900 m, depending on the initial alignment, from the aircraft, and a correction can be applied. Note that there is no correction for the overlap function in the data presented below and the extinction profiles are limited where full overlap is achieved at a range of 2 km below the aircraft.

$$\alpha_a = -\frac{1}{2}\frac{\partial}{\partial r}\ln\left(\frac{P_{i2}^{\parallel} r^2}{\Psi F \beta_m^{\parallel}}\right) - \alpha_m, \tag{7}$$

$$\alpha_m = N\sigma. \tag{8}$$

The 532 nm extinction-to-backscatter ratio (lidar ratio) is simply given by the ratio of the above derived products:

$$S_a = \frac{\alpha_a}{\beta_a}. \tag{9}$$

The aerosol backscatter coefficient for 1064 nm is obtained using an estimate for the value of the lidar ratio and a calibration for the aerosol backscatter coefficient at a given range r_c [6,38,39]:

$$\beta_a = \frac{X_0(r)}{\frac{X(r_c)}{(\beta_m(r_c)+\beta_a(r_c))} - 2S_a\left[\int_{r_c}^{r} X_0(r)\right]} - \beta_m, \tag{10}$$

$$X \equiv (P_{\mathrm{tot}}^{\parallel} + P_{\mathrm{tot}}^{\perp}/G_{\mathrm{dep}})r^2 = (\beta_m + \beta_a)T^2 C_{\mathrm{tot}}^{\parallel}, \tag{11}$$

$$X_0(r) \equiv X(r)\exp\left[-2(S_a - S_m)\int_{r_c}^{r} \beta_m(r')\mathrm{d}r'\right]. \tag{12}$$

Currently, the value of the 1064 nm backscatter coefficient for the calibration range is estimated from the 532 nm backscattered signal in low aerosol loading regions, $\beta_a(532\,\mathrm{nm})/\beta_m(532\,\mathrm{nm}) < 0.05$, using an assumed backscatter coefficient color ratio, $\beta_a(1064\,\mathrm{nm})/\beta_a(532\,\mathrm{nm}) = 0.4$, in nearly clear air regions. The extinction-to-backscatter ratio is assumed in the retrieval as an independent input. Currently, a constant value for S_a is assumed but more sophisticated algorithms could be implemented in future versions, incorporating assumptions on aerosol type inferred from the 532 nm S_a and aerosol depolarization ratio.

The wavelength dependence [40] of the backscattered signal, WVD, is defined in Eq. (13):

$$\mathrm{WVD} = \frac{-\ln\left(\frac{\beta_a(1064\,\mathrm{nm})}{\beta_a(532\,\mathrm{nm})}\right)}{\ln(2)}. \tag{13}$$

The volume depolarization ratio for both wavelengths is measured in the system and determined similarly [41] from Eq. (14).

$$\delta \equiv \frac{(\beta_m^{\perp} + \beta_a^{\perp})}{(\beta_m^{\parallel} + \beta_a^{\parallel})}, \qquad \delta = \frac{P_{\mathrm{tot}}^{\perp}}{P_{\mathrm{tot}}^{\parallel}}\frac{1}{G_{\mathrm{dep}}}. \tag{14}$$

Using the backscatter coefficients and the volume depolarization ratio, the estimated molecular depolarization ratio δ_m, and the aerosol scattering ratio R, the aerosol depolarization ratio δ_a is calculated as follows [41]:

$$\delta_a \equiv \frac{\beta_a^{\perp}}{\beta_a^{\parallel}} = \frac{R\delta(\delta_m + 1) - \delta_m(\delta + 1)}{R(\delta_m + 1) - (\delta + 1)}, \tag{15}$$

where

$$R \equiv \frac{\beta_m + \beta_a}{\beta_m}. \tag{16}$$

5. Calibration Procedures

Significant and critical engineering designs were implemented to provide a set of internally-calibrated measurements that could be performed during flight in relatively short times (<5 min. total). This section provides details on the methodology and implementation of the various calibrations used for the aerosol backscatter and extinction coefficient measurements at 532 nm and the calibration process implemented for the depolarization ratio measurements at both 532 nm and 1064 nm. In particular, the measurement of the iodine filter transmission characterizations,

the gain ratios between channels G_{i2} and G_{dep}, listed in Section 4, and the boresight calibration are described.

A. Iodine Filter Transmission Spectrum

Figure 10 shows a layout of the iodine filter and detector module that interfaces to the fiber-coupled output from the 532 nm *molecular* science channel. The absolute transmission of the iodine filter is required to derive the aerosol backscatter coefficients as described in Eq. (4). The absolute filter transmission spectrum is periodically measured either before or after flights and has been demonstrated to be extremely stable over three years. The 38 × 100 mm iodine cell is manufactured as a "starved" cell [35,42], such that the total quantity of iodine in the cell is limited so as to ensure that all the iodine is in the gas phase at the designed operating temperature (65 °C in this case). This configuration provides less temperature sensitivity and excellent long-term stability [42] compared to earlier published filter designs used in lidar systems [10,15]. The CW 532 nm output from the seed laser is used to measure the absolute transmission of the cell as a function of wavelength to determine the factor F in Eq. (4).

While the absolute transmission spectrum of the iodine cell is required for the 532 nm backscattered signal measurement, the extinction measurement requires only a relative transmission spectrum since it is derived from the derivative of the natural logarithm, as described in Eq. (7). The iodine cell is mounted on a motorized linear stage that moves the cell from the science channel position into a calibration position shown as a dashed line in Fig. 10. While in the calibration position, approximately 2 mW of CW 532 nm light is fiber-coupled into the cell using the 532 nm output of the seed laser. The light is collimated to approximately the same size as the science channel beam and then is passed through a wedge/Lyot depolarizer to eliminate any potential polarization sensitivity in the calibration measurement. The light is then split, 50/50, into two channels using a nonpolarizing beam splitting cube (NPBS): one channel is transmitted through the iodine cell and onto a PIN photodiode and the other is free-space coupled to a similar detector to provide a signal with which to normalize fluctuations in laser energy over the course of the spectral scan of the iodine filter. The seed laser is scanned in frequency over ~12 GHz centered about the operational wavelength of the system (532.242 nm) and the frequency scaling of the scan is determined using a confocal Fabry–Perot interferometer (FPI) with a free spectral range of 600 MHz. The FPI is a commercial unit with mirrors optimized for 1064 nm, a fiber-coupled input, and a built in photodiode and is located in a rack mount box next to the iodine cell. After this frequency scan, the cell is moved back into the science channel position and another scan is performed to determine the relative efficiency between the two PIN photodiodes. An example of the measured frequency-scaled iodine transmission spectra for the main science channel is included in Fig. 7(a).

Table 3. Iodine Vapor Filter Transmission Data Showing Long-Term Stability.

Date	Molecular Transmission (275 K, 0.75 atm)	Difference Relative to Mean
15 September 2004	28.9%	0.3%
14 October 2005	28.4%	−0.2%
24 April 2006	28.5%	−0.1%
18 August 2006	28.5%	−0.1%
Average	28.6%	N/A

The iodine filter implemented in the receiver has a measured online (532.242 nm) transmission of $<10^{-6}$ which provides more than sufficient attenuation of unbroadened aerosol backscattered signal. Additional aerosol backscattered signal outside the iodine absorption line due to spectral impurity could violate the implicit assumption that the molecular backscatter channel contains no aerosol backscattered signal in Eqs. (1) and (6). However, as discussed previously, the spectral purity of the transmitter is monitored on a pulse-by-pulse basis to ensure that the molecular backscatter channel is not contaminated by aerosol and cloud backscattered signal.

The integrated transmission of the molecular backscattered signal through the cell for this system is ~29% at a reference temperature and pressure of 275 K, 0.75 atm., respectively, and has been shown to be constant (absolute change <0.3%) over a two year period. Table 3 shows several measurements made over the ~2 year period. The stability of the iodine filter shows that the iodine number density within the cell is nearly constant. The iodine filter module is sealed and fiber-coupled to the receiver telescope, preventing contaminants from depositing on the cell window and thereby changing the overall transmission.

B. Backscatter Coefficient and Depolarization Gain Calibration

The relative signal strength measured between the molecular and total scattering channels, G_{i2} and the two depolarization channels, G_{dep}, must be determined to calculate the aerosol backscatter coefficient as shown in Eq. (4). The gain ratios depend on the relative optical efficiency and the detector and electronic gain of the two channels. In this system, the electronic gain is adjustable to optimize the dynamic range of the measurements, and gain calibration is required after a change in the electronic gain. In addition, the calibration is typically performed ~2–3 times during a flight to assess the gain stability. Typically, we see a small drift in the gain ratios in the first half hour of the flight as the system is warming up (<1%) and no measurable changes after that point.

For the gain calibration ratio, G_{i2}, in Eq. (5), between the molecular and parallel polarization

channel, the iodine filter is moved into the calibration position shown as the dotted line in Fig. 10, (the same position used to measure the filter transmission spectrum). In this configuration, the molecular and 532 nm parallel channels measure the same backscattered signal (i.e., molecular plus aerosol/cloud backscatter) but with different optical and detector efficiencies. Atmospheric backscattered data is acquired for approximately 1 min, averaged, and ratios between the two channels as a function of range are computed to determine G_{i2}. This ratio has been very constant over the course of multiple flights when the electronic gain is not adjusted. For the 27 flights conducted over the 33 day GoMACCS/TexAQS field campaign, the calibration changed by less than 1.5%, and the average change in the calibration over the course of a single flight varied by 0.3% on average. The calibration ratio is typically measured at least twice per flight, although during this campaign the calibration showed a very high degree of stability, and we relaxed the requirement to a single calibration per flight later in the campaign. The stability in the gain ratio was similar during the MILAGRO mission.

The depolarization calibration ratio between the parallel and perpendicular channels is measured one or more times on each flight following the G_{i2} calibration. Also, as part of the instrument setup, the polarization axis of the outgoing light is matched to that of the receiver following an approach similar to that outlined by Alvarez *et al.* [43]. This operation is repeated prior to every polarization gain ratio calibration. The alignment of transmitter and receiver polarization axes is automated and typically takes less than 1.5 min. The alignment is repeatable and stable to within $<0.1°$ after the system has warmed up. The gain ratio calibration is performed by rotating the transmitted polarization 45° to the receiver analyzer, such that both polarization channels measure equal components of the parallel and perpendicular backscattered return. The time to rotate the half-waveplate and acquire the data is less than 1.5 min. During the entire GoMACCS field campaign, changes in the depolarization gain ratio measurement made at 532 nm (1064 nm) were 2.2% (4.6%), and average changes over a single flight were 1.35% (2.6%). The larger variations in the 1064 nm calibration are believed to be due to noise in the measurement, as the 1064 nm signal has a much lower signal-to-noise ratio than that at 532 nm. The relatively small changes in the calibration ratios over the course of a month-long field mission demonstrates the exceptional stability of the instrument under the significant temperature and pressure changes associated with the aircraft environment.

C. Boresight Calibration Scan

Two calibration procedures are associated with the autonomous boresighting subsystem. The first calibration procedure involves equalizing the boresight detector gains and offsets to simplify the interpretation of the boresight error signals generated by the system. To accomplish this, the quad-fiber bundle is inserted into a custom-built optical fixture that provides a spatially uniform LED light source on all four quadrants, and amplifier gains and offsets are adjusted accordingly. The boresight PMT detectors and electronics are identical to the 532 nm science detectors and achieve the same high degree of gain stability. The second calibration procedure involves centering the quad-fiber bundle on the image of the telescope field stop. To accomplish this, the laser is first steered to the last known aligned position using the Mad City Labs piezo-actuated mirror stage. The output beam is then scanned across the FOV of the receiver by $\pm 400\,\mu$rad in the two orthogonal scan directions of the mirror stage. During this scan, data from the science channels are recorded as a function of scan angle and used to determine the piezo-actuator position that centers the transmitted beam on the receiver FOV. This part of the procedure requires horizontally homogeneous and cloud-free conditions between the aircraft and the farthest range over which the science data are averaged to ensure that the changing backscattered signal conditions do not create an error in determining the aligned position. The piezo-actuator is set to this aligned position and the relative amplitude of the four boresight channels is examined. If the signals are approximately equal, the position of the fiber bundle is aligned accordingly using set screws that translate it in orthogonal directions across the image of the telescope field stop until the amplitudes of the boresight detector are balanced. This alignment procedure is typically only required after the field stop has been changed or reinstalled in the aft-optics.

Under nominal data collection operations, the boresight susbsystem provides an adjustment to the transmitter pointing every few seconds, if required. Experience has shown that the transmitter-to-receiver alignment slowly drifts over the course of a flight by approximately $150\,\mu$rad in both steering axes, presumably due to thermo-elastic effects in the system. The boresight system accurately tracks and corrects for this drift. Without the steering correction applied by the boresight subsystem, the drifting alignment would significantly change the overlap function of the instrument for even the largest operational FOV of 1 mrad and affect the calculations of the 532 nm aerosol extinction and 1064 nm data products in the first several kilometers from the aircraft. The accurate, near real-time beam steering correction feature ensures that the transmitter-to-receiver overlap function is stable and should allow us to model and correct for the overlap in the very near range (0–2 km). Along with maintaining a constant overlap function, the boresight subsystem greatly simplifies operation during flight, eliminating the need to manually assess and tune the alignment of the transmitter to the receiver and the subsequent loss of data that such assessments and alignments would necessitate.

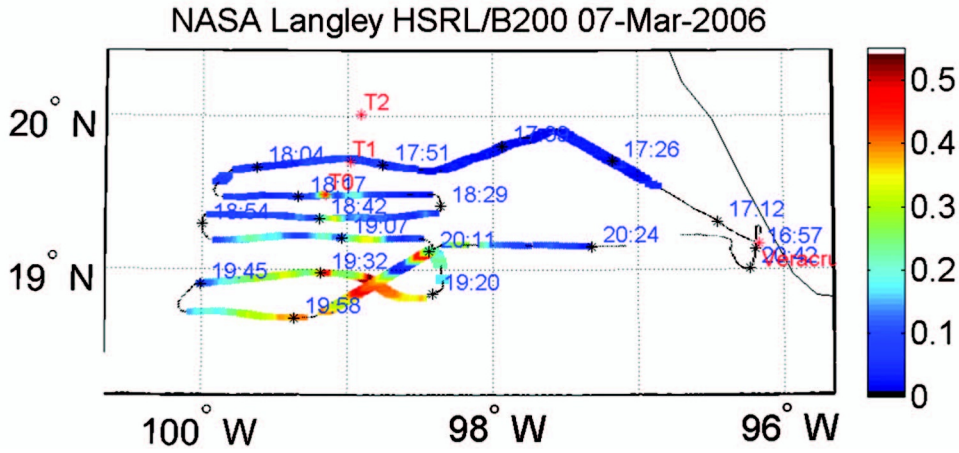

Fig. 11. Flight track over the Mexico City basin for sortie flown on 7 March 2006 based from Veracruz, Mexico. The flight track is color coded with the aerosol optical depth (532 nm) measured with the Airborne HSRL instrument and the time stamp (UT) is denoted along the track. The T1–T2 markers denote the ground-based sites near the Mexico City metropolitan area that were operational during the field deployment.

6. Measurement Results

The airborne HSRL instrument was deployed on the NASA LaRC King Air B-200 in nine major field campaigns since inception. Here we show results from the first mission. The first deployment was for the INTEX-B/MAX-Mex/MILAGRO field campaign which focused on pollution over Mexico City and its outflow and evolution. During MILAGRO, data were collected and analyzed for 19 flights on 15 days. Most of the flights were conducted in coordination with other participating aircraft and heavily instrumented ground-based measurement sites in and near Mexico City. The HSRL flights mostly targeted the Mexico City Basin and nearby region, although several flights were designed to study regional transport of aerosols from Mexico City. The airborne HSRL instrument worked exceptionally well, without requiring maintenance or any realignments or adjustments throughout the entire campaign. In this section we provide an example of the airborne HSRL data to demonstrate the system capability and measurement quality. The ground track for the flight on 7 March 2006 over the Mexico City Basin centered around 19:00 UT (1:00 p.m. local time (LT)) is shown in Fig. 11 and is color coded by the measured aerosol optical thickness. Figure 12 shows the aerosol backscattered profiles measured during this same flight. This particular flight was designed to observe aerosols in the Mexico City basin and outflow to the south, with several transects flown in a raster pattern in a predominately east–west direction over the targeted area. On this flight, the aerosol loading was observed to be higher on the southern portion of the operating area.

Figure 13 presents the compilation of HSRL data products for the flight leg highlighted by the rectangular box in Fig. 12. The data from this flight leg demonstrate the power of the airborne HSRL for observing the spatial distribution of aerosol, quantifying aerosol optical parameters, and inferring aerosol

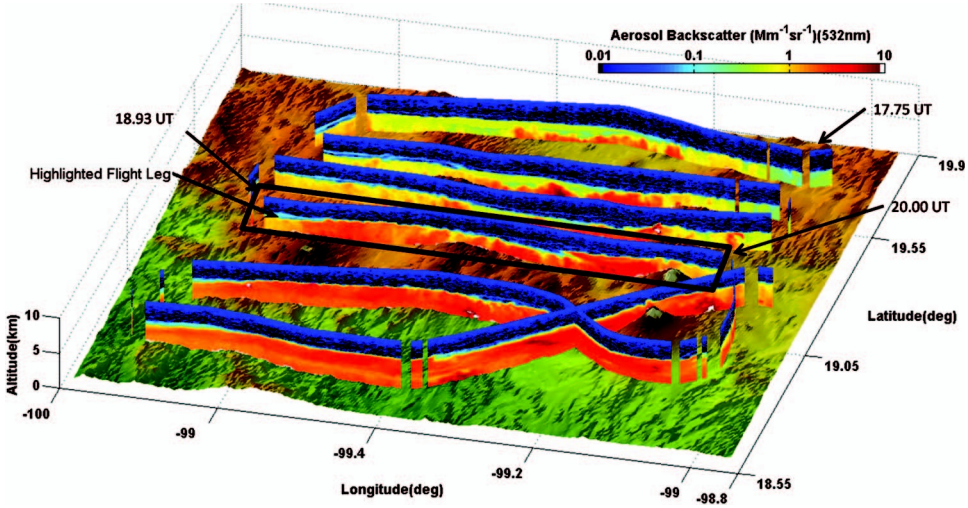

Fig. 12. Flight summary plot of the HSRL aerosol backscattered data taken on 7 March 2006 centered on the Mexico City basin. The particular flight leg shown in Fig. 13 is highlighted.

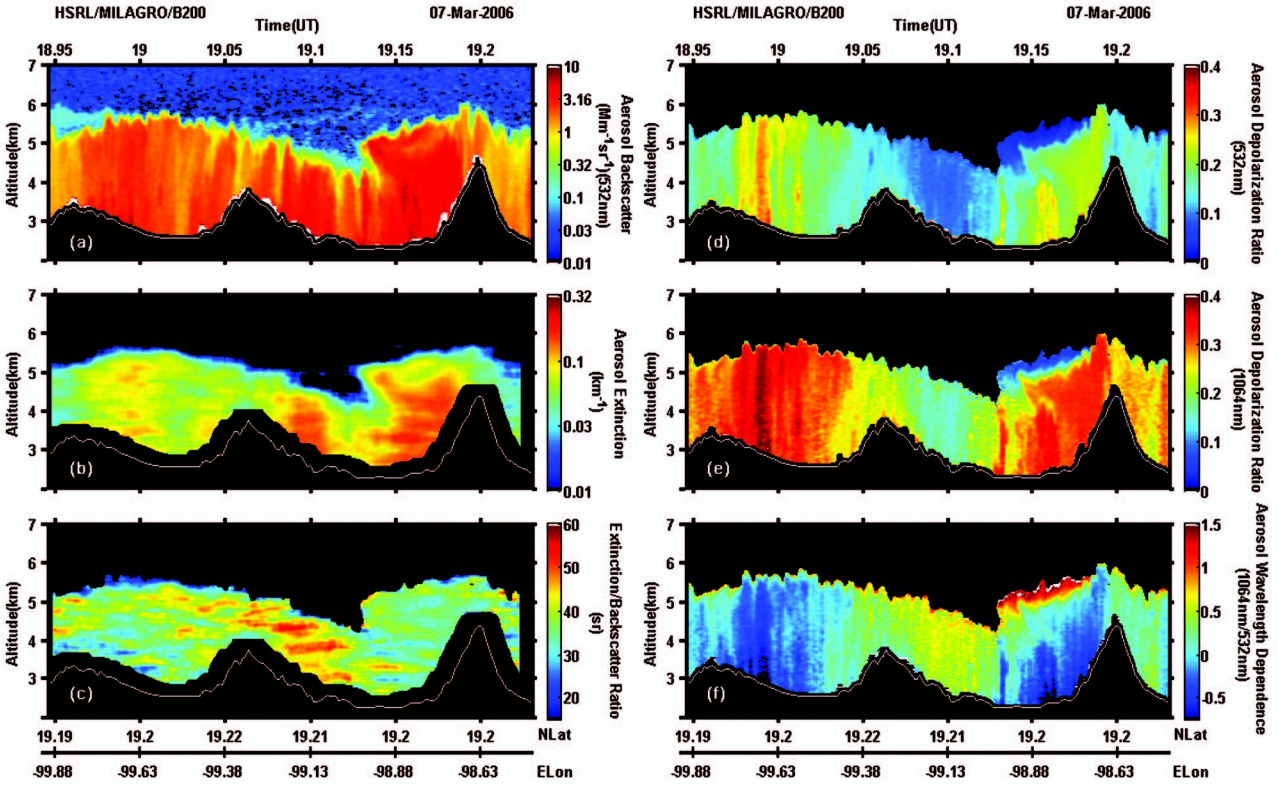

Fig. 13. Flight leg depicted in Fig. 12 showing all of the measurement parameters measured with the HSRL instrument as a function of altitude above mean sea level. The backscatter coefficient, depolarization ratios, and wavelength dependence have 60 m vertical and ~1 km horizontal resolution. The extinction coefficient and extinction-to-backscatter ratio are averaged to a 300 m vertical and ~6 km horizontal resolution.

type. The extensive parameters (dependent on aerosol concentration and type) measured with the high spectral resolution technique are aerosol backscatter and aerosol extinction coefficients at 532 nm, and are shown in Figs. 13(a) and 13(b). The backscatter data is averaged over 10 s (~1 km horizontal resolution)

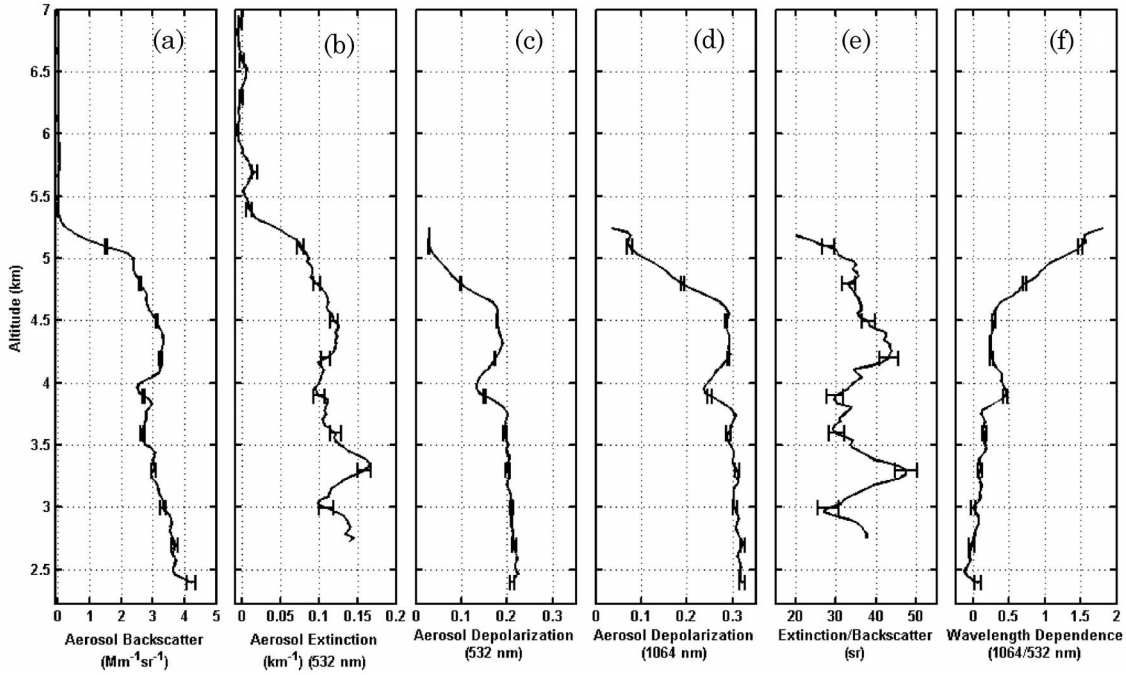

Fig. 14. HSRL measurement profiles plotted above mean seal level at 19:09 UT on 7 March 2006. The minimum altitude plotted, 2.27 km, is set at the ground level for this location. Error bars on all plot represents the shot noise 1 σ standard deviations for the same average resolutions as Fig. 13.

Table 4. Errors Due to Shot Noise for Data Presented in Fig. 14 at 3 km Altitude[a]

Data Product	Mean Value	Standard Deviation	Percent Error
Aerosol backscatter 532 nm (Mm^{-1} sr^{-1})	3.32	0.16	4.8%
Aerosol extinction 532 nm (km^{-1})	0.11	0.01	9%
Aerosol depolarization ratio 532 nm	0.21	0.004	2%
Aerosol depolarization ratio 1064 nm	0.31	0.01	3%
Extinction/backscatter ratio 532 nm	28	2.6	9%
Aerosol wavelength dependence (1064 nm/532 nm)	0.0	0.003	N/A[b]

[a]Spatial resolutions: backscatter coefficient, depolarization ratios, and wavelength dependence 60 m vertical, ~1 km horizontal. The extinction coefficient and extinction-to-backscatter ratio 300 m vertical, ~6 km horizontal.
[b]This is computed in the logarithm domain.

and 60 m in altitude, and the extinction is analyzed over 60 s (~6 km horizontal resolution) and 300 m in altitude. The intensive parameters (dependent only on aerosol type, size, and shape) measured by the HSRL instrument are shown in Figs. 13(c)–13(f) and include aerosol depolarization ratio at both wavelengths (532 nm and 1064 nm) (10 s, 60 m), the aerosol extinction-to-backscatter ratio (S_a) (60 s, 300 m), and the aerosol backscattered signal wavelength dependence (WVD) (10 s, 60 m). The intensive parameters are limited to regions where the aerosol scattering ratio β_a/β_m is >0.2 in this analysis. To avoid contamination of the data products from the effects of the surface returns, the data are limited to 90 m (2 range bins) above the highest ground elevation in the horizontal averaging interval as determined by a digital elevation map. The surface elevation is plotted as a white line in the data products. The surface elevation over the Mexico City region is highly variable and thus requires use of a higher offset from the surface elevation than would be required to process data over a region with flatter topography.

The unambiguous measurement of extinction is the extensive parameter made possible by the HSRL technique. Also, because of the internal calibration of the instrument and the concomitant measurement of extinction, the aerosol backscatter coefficient measurement at 532 nm is much more accurate than can be achieved with a standard backscatter lidar. The curtain profiles of extinction and backscatter coefficients show the distribution of aerosol and are being used to assess the predictions of various transport models. The extinction data are being used to determine aerosol optical depth and compare the HSRL-derived aerosol optical depth to that derived from passive satellite- and aircraft-based sensors, and the backscatter coefficient measurements are being used to independently assess the lidar measurements on the CALIPSO satellite.

The intensive observables from the airborne HSRL have been extremely valuable for mapping the distribution of aerosol by type in the complex atmosphere encountered on MILAGRO. The aerosol depolarization shows high values within the Mexico City region with peak values near 40% (1064 nm) and 35% (532 nm), suggesting that the aerosol loading in these layers was mostly dominated by dust, which was frequently observed during the MILAGRO campaign. Elevated (>5%) depolarization values were typically observed throughout the Mexico City region, indicating a significant dust component to the aerosol in the region. An anticorrelation between the WVD and the aerosol depolarization was observed with WVD values as small as −0.4 for regions with the highest depolarization ratios. The S_a values are higher (50–60 sr) on the western side of the Mexico City basin and show enhancements flowing out over the western mountain range along the basin. This region also shows lower aerosol depolarization and higher WVD, more consistent with urban aerosols. The depolarization is much smaller between 5 and 5.5 km near 19:15 UT at the top of the mixed layer with much higher WVD (~2) and has enhanced S_a (>60 sr), consistent with the biomass burning aerosols observed near the surface during flights early in the mission.

The six plots in Fig. 14 show the vertical profiles of the HSRL measurements at 19.15 UT during the same flight leg as that presented in Fig. 13. The aerosol backscatter and extinction coefficients are presented in (a) and (b). Note that the aerosol extinction above 5.7 km is between $+/-0.005$ km^{-1}, which is on the order of the molecular extinction and provides a measure of the lower bound on the measurement uncertainty for the horizontal and vertical average used. The error bars represent the shot noise variability of the data based on calculations using a noise scale factor method as outlined in Liu *et al.* [44]. For reference, the errors at 3 km altitude at these aerosol loading levels are listed in Table 4. Additional intercomparisons of the HSRL data to other aircraft *in situ* and ground-based remote and *in situ* measurements from MILAGRO will be the focus of near-term future publications.

7. Systematic Errors

An analysis of the systematic errors for all data products from the airborne HSRL is beyond the scope of this paper. A manuscript focused on a complete error analysis and validation of extinction measurements is currently in preparation. Here we provide a brief overview of the main systematic errors in the HSRL measurement at 532 nm. The main sources of systematic errors in the 532 nm measurement arise from the spectral characteristics of the laser and

iodine filter transmission, calibration errors, and inputs of the atmospheric density and temperature. These sources of error impact the retrievals of both aerosol backscatter and extinction. We first address the impact on the error in backscatter.

For standard backscatter lidars, the aerosol backscatter coefficient retrieval typically relies on calibrating the measured signals to so-called "clear air" regions, i.e., regions assumed to exhibit low aerosol loading and for which the backscatter coefficient can be considered insignificant or estimated with sufficient accuracy. The problem with this technique is that nature does not always provide aerosol-free regions, even in the free troposphere, and regions that appear to be free of aerosol can contain background aerosol of significant backscatter strength. Our observations frequently show that the background aerosols extend up to the altitude of the aircraft (typically 9 km) with backscatter ratios (β_a/β_m) greater than 10%. Therefore, for a consistent, accurate calibration that is independent of *a priori* assumptions on aerosol loading, the internal calibration technique outlined in Section 5 has been implemented. The systematic errors in the aerosol backscatter coefficient derived from Eq. (4) arise from the measurements of the absolute transmission of the iodine filter (F), gain calibrations (G_{i2} and G_{dep}), and the molecular depolarization (δ_m). In addition, systematic errors related to the spectral purity of the transmitter and to the transmission of the iodine filter at the laser wavelength must also be considered.

The estimated errors in the two gain calibrations G_{i2} and G_{dep} are quite small: 0.3% and 1.35%, respectively, at 532 nm; these errors induce a fractional uncertainty in the backscatter ranging from 0.3%–0.74% depending on the magnitude of the aerosol depolarization.

The transmission of the iodine filter is stable and known to high accuracy; hence calibration errors associated with that factor are also small. The measured absolute transmission of the iodine filter has varied by less than 0.3% over a period of two years. The transmission of the molecular Cabannes scattering through the filter depends on both atmospheric temperature and pressure, but is far more sensitive to temperature. Even so, the sensitivity of the molecular scattering transmission to atmospheric temperature is only 0.36%/K for the iodine line at which the system is operated. The atmospheric temperature profile used in the retrievals is derived from NASA's Global Modeling and Assimilation Office (GMAO), and therefore the errors in backscatter due to temperature errors vary based on the location and time of the measurements. We assume the atmospheric temperature error to be 3° based on previous analysis [23]. Under this assumption, the error in the molecular backscatter coefficient is ~1%, and the error in the transmission of the backscattered signal through the iodine filter due to the uncertainty of the atmospheric temperature is 1.1%.

The error arising from uncertainty in the molecular depolarization is also quite small. Given the bandwidth of the interference filter and etalon in the HSRL (transmitting Cabannes spectrum only), the theoretical value of the molecular depolarization is 0.0036. However, the molecular depolarization estimated from observations is over twice that at 0.008 ± 0.002, which is reasonable as we expect some degree of polarization cross talk in the receiver. (The molecular depolarization values are determined from clear air regions that have aerosol scattering ratios, β_a/β_m, less than ~2%.) Using the error in molecular depolarization derived from the observations, the error induced in the aerosol backscatter measurement is estimated to be 0.2%.

The spectral purity of the transmitter and transmission of the iodine filter at line center determine the degree to which aerosol backscatter contaminates the assumed Cabannes backscatter measured downstream of the iodine filter. The spectral purity ratio, defined above, is greater than 5000:1, and the iodine filter transmission is 10^{-6} at the transmitted laser frequency. The induced systematic error in backscatter arising from aerosol contamination in the molecular channel is less than 0.03% and 0.3% for aerosol scattering ratios less than 15 and 150, respectively.

Overall, the combined systematic error in the aerosol backscattering coefficient associated with the gain calibrations, iodine filter transmission, spectral purity, atmospheric state parameters, and molecular depolarization is estimated to be less than 2.3%, assuming aerosol scattering ratios less than 150 and error in the atmospheric temperature less than 3°.

Systematic errors in the derived aerosol extinction coefficient from Eq. (7) arise from the errors in the laser spectral purity, iodine filter transmission, atmospheric state parameters, and the transmitter-to-receiver optical overlap function (note that the 532 nm aerosol backscatter coefficient retrieval is not affected by the overlap function). As stated above, the extinction coefficient is currently limited to ranges (2–2.5 km) away from the lidar where the overlap is constant for the results presented. Taking advantage of the transmitter-to-receiver alignment stability achieved by the autonomous boresighting system, we are currently updating our algorithms to estimate and correct for the overlap function so that extinction is calculated closer to the aircraft; those results will be presented in a later publication. As in the Raman lidar technique, the aerosol extinction coefficient is estimated from difference between the observed attenuated molecular backscattering profile and the unattenuated backscatter profile that is estimated from a model-derived profile of air density. As such, the systematic errors in extinction associated with uncertainties in the density profile are the same as those that have been documented for Raman lidar systems. Ansmann *et al.* [24] have presented errors in the extinction coefficient due to the presence of temperature inversions not accounted for

in the model-derived density profile. The errors in aerosol extinction ranged between 0.015 and $0.025\,km^{-1}$ for actual lapse rates differing by 7 to 37 K/km from the model-derived lapse rates. The magnitude of the systematic errors depends on the depth of the inversion and the vertical resolution of the measurements.

Temperature inversions not accounted for in model-derived state parameters also lead to errors in the estimate of the transmission through the iodine filter (F) that is used in the extinction retrieval; however, these errors are small due to the low sensitivity to atmospheric temperature outlined above in the discussion of aerosol backscatter errors.

The systematic error due to the spectral purity of the laser is dependent on both the magnitude of and vertical gradients in the aerosol scattering ratio. For example, for a change in aerosol backscatter ratio by a factor of 10 over 300 m (i.e., transition from clean air to a very strong aerosol plume), the magnitude of the error in the aerosol extinction coefficient is less than $0.01\,km^{-1}$ given the spectral purity of our laser. For clouds the extinction error can be higher, e.g., an error of $0.11\,km^{-1}$ assuming a factor of 100 change in scattering ratio over 300 m; however the induced relative error in extinction is quite small.

The example estimates of systematic errors in extinction noted above assume very strong, and hence rare, gradients in the atmospheric temperature and aerosol loading. For typical conditions, the systematic error in the extinction coefficient is much less than the random errors, i.e., less than $0.01\,km^{-1}$, for the LaRC HSRL instrument.

Other potential sources of systematic errors, such as corrections for Doppler shifts due to the aircraft motion, laser locking stability, and frequency offsets of the pulsed and seed laser, have been examined and found to introduce small ($<1\%$) errors in the derived aerosol backscatter and extinction coefficients.

8. Summary

The NASA LaRC airborne HSRL instrument has proven to be extremely robust. The transmitter subsystem was carefully designed to ensure that the laser output frequency is locked to a known location on the iodine absorption line, and the spectral purity of the output pulses is monitored on a shot-by-shot basis, thereby eliminating the possibility of systematic problems with the implementation of the HSRL technique and subsequent structural error in the data products. Measurements show that the laser reliably seeds at the desired wavelength and achieves spectral purity greater than 5000:1 in the vibrational environment of the aircraft. The unique internal radiometric calibration of the receiver ensures the accuracy of the aerosol intensive and extensive data products, and results from laboratory tests and past field missions have demonstrated the remarkable stability of the instrument. The analysis of the iodine filter transmission demonstrated changes of less than 0.3% over the course of two years and the overall gain ratio between the aerosol and molecular backscatter channels was assessed to change less than 0.3% within a flight and less than 1.35% over an entire month-long field campaign. Variation in the polarization gain ratio was measured to be less than 1.35% (2.6%) on each flight for the 532 nm (1064 nm) wavelengths. To date, the instrument has flown over 650 flight hours with minimal maintenance. Data products from nine major field experiments have been archived and are being used in various scientific studies, including investigations of aerosol properties and aerosol-cloud interactions, satellite validation, assessment of chemical transport models, and investigation of new lidar retrieval techniques. Currently, a complete assessment of the measurement errors and intercomparisons of the airborne HSRL measurements to airborne *in situ* aerosol and sun photometer measurements of aerosol extinction is in preparation. Initial measurement comparisons have been presented at conferences and workshops and show excellent agreement [45].

The authors thank the two reviewers for their detailed reviews that improved the manuscript. We also acknowledge the support of the NASA LaRC, NASA HQ Science Mission Directorate, and the NASA CALIPSO Project for funding the development of the HSRL instrument. The deployment of the HSRL in these field experiments were supported in part by the U.S. Department of Energy's Atmospheric Science Program (Office of Science, BER, Grant DE-AI02-05ER63985). We also acknowledge the aircraft flight support provided by personnel in the NASA LaRC Research Services Directorate.

References

1. Intergovernmental Panel on Climate Change, *Climate Change 2007: The Physical Science Basis: Contribution of Working Group I to the Fourth Assessment Report of the IPCC*, S. Solomon, D. Qin, M. Manning, Z. Chen, M. Marquis, K. B. Averyt, M. Tignor, and H. L. Miller, eds. (Cambridge University, 2007), pp. 996.
2. D. B. Harper, A. Cook, C. Hostetler, J. W. Hair, and T. L. Mack, "NASA Langley airborne High Spectral Resolution Lidar instrument description," in *Proceedings of 23rd International Laser Radar Conference*, C. Nagasawa and N. Sugimoto, eds. (ILRC, 2006), p. PD1-5.
3. J. W. Hair, C. A. Hostetler, R. A. Ferrare, A. L. Cook, and D. B. Harper, "The NASA Langley Airborne High Spectral Resolution Lidar for Measurements of Aerosols and Clouds," in *Proceedings of 23rd International Laser Radar Conference*, C. Nagasawa and N. Sugimoto, eds. (ILRC, 2006), pp. 411–414.
4. J. D. Klett, "Stable analytical inversion solution for processing lidar returns," Appl. Opt. **20**, 211–220 (1981).
5. J. D. Klett, "Lidar inversion with variable backscatter/extinction ratios," Appl. Opt. **24**, 1638–1643 (1985).
6. F. G. Fernald, B. M. Herman, and J. A. Reagan, "Determination of aerosol height distributions by lidar," J. Appl. Meteorol. **11**, 482–489 (1972).
7. Z. Liu, N. Sugimoto, and T. Murayama, "Extinction-to-backscatter ratio of Asian dust observed with high-spectral-resolution lidar and Raman lidar," Appl. Opt. **41**, 2760–2767 (2002).
8. D. Müller, A. Ansmann, I. Mattis, M. Tesche, U. Wandinger, D. Althausen, and G. Pisani, "Aerosol-type-dependent lidar

ratios observed with Raman lidar," J. Geophys. Res. **112**, D16202 (2007), doi:10.1029/2006JD008292..
9. S. T. Shipley, D. H. Tracy, E. W. Eloranta, J. T. Tauger, J. T. Sroga, F. L. Roesler, and J. A. Weinman, "High spectral resolution lidar to measure optical scattering properties of atmospheric aerosols. 1: Theory and instrumentation," Appl. Opt. **22**, 3716–3724 (1983).
10. P. Piironen and E. W. Eloranta, "Demonstration of a high-spectral-resolution lidar based on an iodine absorption filter," Opt. Lett. **19**, 234–236 (1994).
11. C. J. Grund and E. W. Eloranta, "University of Wisconsin high spectral resolution lidar," Opt. Eng. **30**, 6–12 (1991).
12. C. Y. She, R. J. Alvarez II, L. M. Caldwell, and D. A. Krueger, "High-spectral-resolution Rayleigh–Mie lidar measurement of aerosol and atmospheric profiles," Opt. Lett. **17**, 541–543 (1992).
13. D. A. Krueger, L. M. Caldwell, R. J. Alvarez II, and C. Y. She, "Self-consistent method for determining vertical profiles of aerosol and atmospheric properties using a high spectral resolution Rayleigh–Mie lidar," J. Atmos. Ocean. Technol. **10**, 533–545 (1993).
14. R. J. Alvarez II, L. M. Caldwell, Y. H. Li, D. A. Krueger, and C. Y. She, "High-spectral-resolution lidar measurement of tropospheric backscatter-ratio with barium atomic blocking filters," J. Atmos. Oceanic Technol. **7**, 876–881 (1990).
15. J. W. Hair, L. M. Caldwell, D. A. Krueger, and C.-Y. She, "High-spectral-resolution lidar with iodine-vapor filters: measurement of atmospheric-state and aerosol profiles," Appl. Opt. **40**, 5280–5294 (2001).
16. Z. Liu, I. Matsui, and N. Sugimoto, "High-spectral-resolution lidar using an iodine absorption filter for atmospheric measurements," Opt. Eng. **38**, 1661–1670 (1999).
17. J. T. Sroga, E. W. Eloranta, S. T. Shipley, F. L. Roesler, and P. J. Tryon, "High spectral resolution lidar to measure optical scattering properties of atmospheric aerosols. 2: Calibration and data analysis," Appl. Opt. **22**, 3725–3732 (1983).
18. U. Wandinger, D. Müller, C. Böckmann, D. Althausen, V. Matthias, J. Bösenberg, V. Weiss, M. Fiebig, M. Wendisch, A. Stohl, and A. Ansmann, "Optical and microphysical characterization of biomass-burning and industrial-pollution aerosols from multiwavelength lidar and aircraft measurements," J. Geophys. Res. **107**, 8125, doi:10.1029/2000JD000202 (2002).
19. M. Esselborn, M. Wirth, A. Fix, M. Tesche, and G. Ehret, "Airborne high spectral resolution lidar for measuring aerosol extinction and backscatter coefficients," Appl. Opt. **47**, 346–358 (2008).
20. G. Tenti, C. D. Boley, and R. C. Desai, "On the kinetic model description of Rayleigh–Brillouin scattering from molecular gases," Can. J. Phys. **52**, 285–290 (1974).
21. A. T. Young, "Rayleigh scattering," Phys. Today **35**, 42–48 (1982).
22. C.-Y. She, "Spectral structure of laser light scattering revisited: bandwidths of nonresonant scattering lidars," Appl. Opt. **40**, 4875–4884 (2001).
23. P. B. Russell, T. J. Swissler, and M. P. McCormick, "Methodology for error analysis and simulation of lidar aerosol measurements," Appl. Opt. **18**, 3783–3797 (1979).
24. A. Ansmann, M. Riebesell, and C. Weitkamp, "Measurement of atmospheric aerosol extinction profiles with a Raman lidar," Opt. Lett. **15**, 746–748 (1990).
25. F. E. Hovis, M. Rhoades, R. L. Burnham, J. D. Force, T. Schum, B. M. Gentry, H. Chen, S. X. Li, J. W. Hair, A. L. Cook, and C. A. Hostetler, "Single-frequency lasers for remote sensing," Proc. SPIE **5332**, 263–270 (2004).
26. J. N. Forkey, "Development and demonstration of filtered Rayleigh scattering—a laser based flow diagnostic for planar measurement of velocity, temperature and pressure," Ph.D. dissertation (Princeton University, 1996).
27. J. N. Forkey, W. R. Lempert, and R. B. Miles, "Corrected and calibrated I_2 absorption model at frequency-doubled Nd:YAG laser wavelengths," Appl. Opt. **36**, 6729–6738 (1997).
28. S. W. Henderson, E. H. Yuen, and E. S. Fry, "Fast resonance-detection technique for single-frequency operation of injection-seeded Nd:YAG lasers," Opt. Lett. **11**, 715–717 (1986).
29. M. P. Larsen, E. Thomas, T. Walther, and E. S. Fry, "Injection seeding of a Ti:sapphire laser using a ramp-hold-fire technique," in *Conference on Lasers and Electro-Optics* (Optical Society of America, 1997), pp. 3046–3050.
30. T. Walther, M. P. Larsen, and E. S. Fry, "Generation of Fourier-transform-limited 35 ns pulses with a ramp-hold-fire seeding technique in a Ti:sapphire laser," Appl. Opt. **40**, 3046–3050 (2001).
31. E. S. Fry, Q. Hu, and X. Li, "Single frequency operation of an injection-seeded Nd:YAG laser in high noise and vibration environments," Appl. Opt. **30**, 1015–1017 (1991).
32. A. Arie and R. L. Byer, "Frequency stabilization of the 1064 nm Nd:YAG lasers to Doppler-broadened lines of iodine," Appl. Opt. **32**, 7382–7386 (1993).
33. A. Arie, S. Schiller, E. K. Gustafson, and R. L. Byer, "Absolute frequency stabilization of diode-laser-pumped Nd:YAG lasers to hyperfine transitions in molecular iodine," Opt. Lett. **17**, 1204–1206 (1992).
34. G. C. Bjorklund, "Frequency-modulation spectroscopy: a new method for measuring weak absorptions and dispersions," Opt. Lett. **5**, 15–17 (1980).
35. J. Crafton, C. D. Carter, and G. S. Elliott, "Three-component phase-averaged velocity measurements of an optically perturbed supersonic jet using multi-component planar Doppler velocimetry," Meas. Sci. Technol. **12**, 409–419 (2001).
36. A. Bucholtz, "Rayleigh-scattering calculations for the terrestrial atmosphere," Appl. Opt. **34**, 2765–2773 (1995).
37. U. Wandinger and A. Ansmann, "Experimental Determination of the Lidar Overlap Profile with Raman Lidar," Appl. Opt. **41**, 511–514 (2002).
38. P. B. Russell, T. J. Swissler, and M. P. McCormick, "Methodology for error analysis and simulation of lidar aerosol measurements," Appl. Opt. **18**, 3783–3797 (1979).
39. C. Cattrall, J. A. Reagan, K. Thome, and O. Dubovik, "Variability of aerosol and spectral lidar and backscatter and extinction ratios of key aerosol types derived from selected Aerosol Robotic Network locations," J. Geophys. Res. **110**, D10S11 (2005), doi: 10.1029/2004JD005124.
40. Y. Sasano and E. V. Browell, "Light scattering characteristics of various aerosol types derived from multiple wavelength lidar observations," Appl. Opt. **28**, 1670–1679 (1989).
41. F. Cairo, G. Di Donfrancesco, A. Adriani, L. Pulvirenti, and F. Fierli, "Comparison of various linear depolarization parameters measured by lidar," Appl. Opt. **38**, 4425–4432 (1999).
42. T. J. Quinn and J.-M. Chartier, "A new type of iodine cell for stabilized lasers," IEEE Trans. Instrum. Meas. **42**, 405–406 (1993).
43. J. M. Alvarez, M. A. Vaughan, C. A. Hostetler, W. H. Hunt, and D. M. Winker, "Calibration technique for polarization-sensitive lidars," J. Atmos. Oceanic Technol. **23**, 683–699 (2006).
44. Z. Liu, W. Hunt, M. Vaughan, C. Hostetler, M. McGill, K. Powell, D. Winker, and Y. Hu, "Estimating random errors due to shot noise in backscatter lidar observations," Appl. Opt. **45**, 4437–4447 (2006).
45. R. R. Rogers, J. W. Hair, C. A. Hostetler, R. A. Ferrare, A. L. Cook, D. B. Harper, M. D. Obland, S. P. Burton, A. Clarke, Y. Shinozuka, J. Redemann, P. Russell, and J. Livingston, "Evaluation of NASA/LaRC airborne High Spectral Resolution Lidar aerosol extinction measurements," in *Proceedings of the 24th International Laser Radar Conference* (ILRC, 2008), pp. 940–942.